Astron. Astrophys. 164, 415–427 (1986)

ASTRONOMY
AND
ASTROPHYSICS

The scintillation theory of eclipse shadow bands

J.L. Codona

La Jolla Institute, Center for Studies of Nonlinear Dynamics★, 3252 Holiday Court, Suite 208, La Jolla, CA 92037, USA

Received November 28, 1985; accepted January 21, 1986

Summary. The results of a theoretical investigation of solar eclipse shadow bands are presented. The study provides both quantitative and qualitative insight into the factors governing the visibility of shadow bands. Using only standard, weak scattering scintillation theory and standard models for atmospheric turbulence, all of the salient features of the shadow bands are explained. The contrast is found to be greater for shorter wavelengths and the band spacing to scale like the square-root of the wavelength very near totality. For times greater than about 20 seconds before (or after) totality the band spacing becomes frequency independent and the scintillations are dominated by turbulence near the ground. The turbulence mainly responsible for shadow bands is found to be below two kilometers in altitude. Turbulence at the tropopause is found to have no impact on shadow bands until 2–3 seconds from totality. Longer eclipses are expected to show bands with greater contrast and linearity. Intensity correlation scales are typically less than 10 cm within 30 seconds of totality. The scintillation theory predictions for shadow band structure, motion, and evolution are found to be in agreement with both visual and photoelectric observations.

Key words: Earth: atmosphere – eclipses – photometry – scintillation – seeing

1. Introduction

During the few minutes just preceding and just following the occurrence of totality in solar eclipses, faint shadowy patterns have sometimes been seen to appear on the ground (Marschall, 1984). These "shadow bands" are initially seen to be random and disorganized, becoming more linear and aligned with the edge of the lunar shadow as totality approaches. At the same time the band spacing decreases and the contrast increases. The bands appear to move in a direction perpendicular to their elongation (Marschall, 1984). Photoelectric studies have shown that the bands' contrast is greater at shorter wavelengths while, near totality, the typical width of the bands increases with wavelength (Young, 1970b). The phenomena appear to reverse their general trends after totality with the exception of the band motion, which appears to be unrelated to the location of the lunar shadow.

It has long been suggested that shadow bands are most likely a scintillation phenomenon caused by turbulence in the Earth's atmosphere (Minnaert, 1954). However, details such as whether or not and how well shadow bands will be seen, and the wavelength dependence of the bands have not been well understood. The wavelength dependence has been attributed to solar limb darkening (Quann and Daly, 1972). It has been conjectured that the thermal effects of the moon's shadow might possibly cause an increase in atmospheric turbulence (Young, 1970a). In this paper it will be shown that all of the recorded effects of shadow bands can be explained with standard scintillation theory, without the use of limb darkening or enhanced turbulence.

In the next section, the theory for a general, infinitely-distant, extended, incoherent light source illuminating a thin phase screen is reviewed. An expression is presented for the two point intensity correlation, which includes the normalized intensity variance (the scintillation index). In Sect. 3 the specific case of crescent brightness distributions is presented. Section 4 utilizes the thin-screen model to determine the magnitude and wavelength dependence of the shadow-bands' intensity variance. In Sect. 5 the model is used to find the behavior of the intensity spectrum, its dependence on time and wavelength, and its implications for the morphology, orientation, and scales of the shadow bands. In Sect. 6 the theory is generalized to account for distributed atmospheric turbulence. The results of the theory are summarized in Sect. 7 followed by comparisons to observations.

2. The phase screen model

At any given moment, the shadows on the ground may be described as a random intensity pattern, $I(\boldsymbol{x})$, where $\boldsymbol{x}$ is a position vector in the observation plane. For simplicity, we treat the light as essentially monochromatic. This is a good approximation if the light is detected through narrow-band filters, otherwise, integration over the detector bandpass is required. The intensity patterns are assumed to arise from temperature and density fluctuations in the atmosphere and change in a semi-random fashion as the irregularities evolve and are convected by the wind. The random nature of atmospheric turbulence dictates a statistical analysis. A study of the two-point intensity correlation, $C_I(\boldsymbol{s}) = \langle I(\boldsymbol{x})I(\boldsymbol{x}+\boldsymbol{s})\rangle$, lends a great deal of insight

Send offprint requests to: J.L. Codona
★ Affiliated with the University of California, San Diego
★★ Present address: AT&T Bell Laboratories, Whippany Road, Whippany, NJ 07981, USA

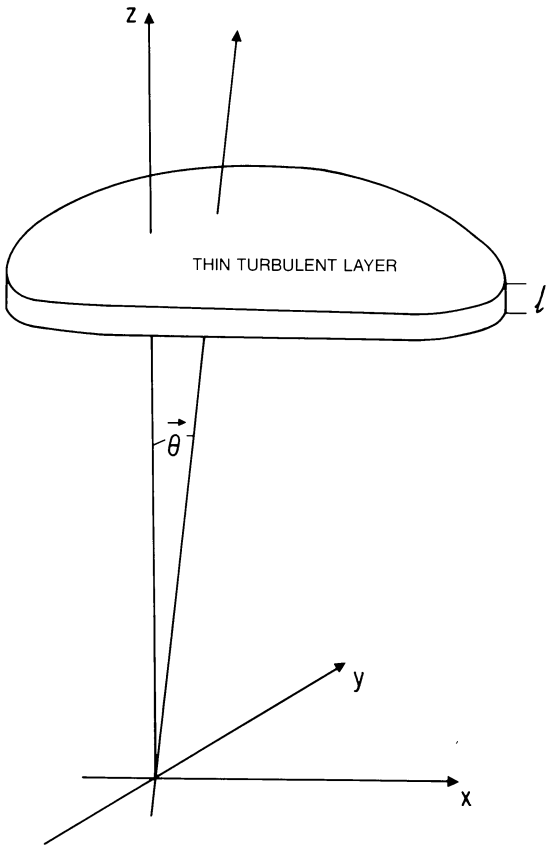

Fig. 1. Geometry for the thin screen model. The ground is at $z = 0$ and l is the thickness of the screen

into the nature of the shadow bands. Angle brackets denote ensemble averaging over fluctuations in the atmosphere. The intensity correlation function allows us to discuss how the shadow bands' contrast and spatial scales vary in time. A convenient measure of the pattern contrast is given by the "scintillation index," m, defined as the rms intensity fluctuations normalized by the mean intensity

$$m^2 = \frac{\langle (I - \langle I \rangle)^2 \rangle}{\langle I \rangle^2} = \frac{C_I(0) - C_I(\infty)}{C_I(\infty)} \tag{1}$$

In this section we review the theory for the intensity correlation resulting from an incoherent source illuminating a weakly-scattering layer of turbulent atmosphere (a thin "phase changing screen") at a distance z from the observer (Fig. 1). Later, since the scattering is weak, we will analyze the effects of extended atmospheric turbulence by superimposing the thin-screen results.

The index of refraction in air, $n(\boldsymbol{r})$, is very near unity. The fluctuations in the index are written $\mu(\boldsymbol{r}) \equiv n(\boldsymbol{r}) - \langle n \rangle$ and are extremely small relative to the mean. These fluctuations are assumed to arise from turbulent processes in the air. The three-dimensional "turbulence spectrum" is defined

$$\Phi_\mu(q) = \frac{1}{(2\pi)^3} \int_{-\infty}^{\infty} \langle \mu(\boldsymbol{r}_0)\mu(\boldsymbol{r}_0 + \boldsymbol{r}) \rangle e^{-i\boldsymbol{q}\cdot\boldsymbol{r}} d^3r \tag{2}$$

where $\boldsymbol{q}$ is a three-dimensional wave vector and the autocovariance of the index of refraction fluctuations, $\langle \mu(\boldsymbol{r}_0)\mu(\boldsymbol{r}_0 + \boldsymbol{r}) \rangle$, is assumed to be homogeneous and isotropic within the turbulent region. For the spatial scales important to scintillations, we treat the turbulence spectrum as a power-law

$$\Phi_\mu(q) = 0.033 C_n^2 q^{-11/3} \tag{3}$$

where C_n^2 is the turbulence structure constant and a Kolmogorov turbulence spectrum has been assumed (Tatarskii, 1971).

Since the solar crescent is incoherent with a brightness distribution, $B(\boldsymbol{\theta})$, the intensity pattern on the ground may be written as the sum of intensities contributed by the various parts of the source

$$I(\boldsymbol{x}) = \int_{-\infty}^{\infty} B(\boldsymbol{\Theta}) I_{pw}(\boldsymbol{x} + z\boldsymbol{\Theta}) d^2\boldsymbol{\Theta} \tag{4}$$

where $I_{pw}(\boldsymbol{x})$ is the intensity pattern that would result from illuminating the thin screen with a normally-incident plane wave (i.e. the intensity pattern that would result from a star at the zenith). A consequence of the paraxial wave approximation (Tatarskii, 1971) is that the intensity pattern shifts by $-z\boldsymbol{\Theta}$ when the direction of incidence of the plane wave is shifted by $\boldsymbol{\Theta}$. Therefore, Eq. (4) shows that the effect of an extended source is to "smudge" the intensity pattern on the ground. Since $B(\boldsymbol{\Theta})$ is zero beyond the edge of the source, the limits of integration may be written as infinite without any difficulty.

$I_{pw}(\boldsymbol{x})$ is a random function of position as is the total intensity pattern, $I(\boldsymbol{x})$. Starting from Eq. (4), we may write the product of the total intensity at two points on the ground and average over fluctuations in the atmosphere to find the intensity correlation

$$C_I(\boldsymbol{s}) = \iint_{-\infty}^{\infty} B(\boldsymbol{\Theta}_1) B(\boldsymbol{\Theta}_2) C_{pw}(\boldsymbol{s} - z(\boldsymbol{\Theta}_1 - \boldsymbol{\Theta}_2)) d^2\Theta_1 d^2\Theta_2 \tag{5}$$

where $C_{pw}(\boldsymbol{s}) = \langle I_{pw}(\boldsymbol{x}) I_{pw}(\boldsymbol{x} + \boldsymbol{s}) \rangle$ and statistical homogeneity has been assumed. Note that regardless of whether $C_{pw}(\boldsymbol{s})$ is isotropic, $C_I(\boldsymbol{s})$ will not be isotropic if $B(\boldsymbol{\Theta})$ is anisotropic. This is why the scintillations of stars and planets are statistically isotropic (Young, 1969) but shadow bands are not. It is often convenient to discuss the power spectrum of the fluctuating intensity (the "intensity spectrum"); defined as

$$\Phi_I(\boldsymbol{\kappa}) = \frac{1}{(2\pi)^2} \int_{-\infty}^{\infty} C_I(\boldsymbol{s}) e^{-i\boldsymbol{\kappa}\cdot\boldsymbol{s}} d^2s \tag{6}$$

where $\boldsymbol{\kappa}$ is the two-dimensional "spatial frequency." Taking the Fourier transform of Eq. (5) leads to

$$\Phi_I(\boldsymbol{\kappa}) = (2\pi)^4 |\tilde{B}(z\boldsymbol{\kappa})|^2 \Phi_{pw}(\boldsymbol{\kappa}) \tag{7}$$

where $\tilde{B}(z\boldsymbol{\kappa})$ is the Fourier transform of the brightness distribution with respect to $\boldsymbol{\Theta}$ and $\Phi_{pw}(\boldsymbol{\kappa})$ is the transform of $C_{pw}(\boldsymbol{s})$. This is the formula for the source averaging of an intensity spectrum by an extended, incoherent source (Salpeter, 1967).

In addition to the source's effect on the intensity spectrum, we must also consider the point source intensity spectrum, $\Phi_{pw}(\boldsymbol{\kappa})$. For a plane wave incident on a weakly scattering thin phase screen, the intensity spectrum is well known (Salpeter, 1967)

$$\Phi_{pw}(\boldsymbol{\kappa}) = \delta(\boldsymbol{\kappa}) + 8\pi k^2 l \sin^2\left(\frac{z\kappa^2}{2k}\right) \Phi_\mu(\boldsymbol{\kappa}) \tag{8}$$

where l is the thickness of the screen, $k = 2\pi/\lambda$, and λ is the wavelength. This is the weak scattering approximation to the intensity spectrum for a point source. The factor $2\sin^2(z\kappa^2/2k)$ is called the "Fresnel filter." The intensity spectrum for an ex-

tended source is found by combining Eqs. (8) and (7) to give

$$\Phi_I(\boldsymbol{\kappa}) = I_{total}^2\,\delta(\boldsymbol{\kappa}) + (2\pi)^4 8\pi k^2 l |\tilde{B}(z\boldsymbol{\kappa})|^2 \sin^2\left(\frac{z\kappa^2}{2k}\right)\Phi_\mu(\boldsymbol{\kappa}) \tag{9}$$

where we have made use of the fact that $(2\pi)^2\tilde{B}(0) = I_{total}$, the total intensity of the extended source. The intensity fluctuation spectrum is the second term in Eq. (9). The intensity correlation is the inverse Fourier transform of Eq. (9). Noting that the total intensity is equal to the mean intensity,

$$\langle I\rangle = \int_{-\infty}^{\infty} B(\boldsymbol{\Theta}) d^2\Theta \equiv I_{total}$$

we find the scintillation index as

$$m^2 = 8\pi k^2 l \int_{-\infty}^{\infty} \frac{|\tilde{B}(z\boldsymbol{\kappa})|^2}{|\tilde{B}(0)|^2} \sin^2\left(\frac{z\kappa^2}{2k}\right)\Phi_\mu(\boldsymbol{\kappa}) d^2\kappa \tag{10}$$

While Eqs. (9) and (10) are valid for essentially any broad source seen through a thin weakly-turbulent layer, the dynamic crescent source distribution makes the special case of shadow bands unique.

3. Crescent source distributions

The very thin solar crescent is responsible for creating the remarkable scintillation effects observed in shadow bands. Its sheer brilliance sets it apart from other scintillating objects in that it may be visually observed by backscattering off the ground. The crescent rapidly changes its shape and size as totality nears; the manner and rate of which are governed by the relative sizes of the sun and moon, which change from one eclipse to the next. In annular eclipses, the crescent even changes its complete nature, from a crescent to a ring.

In order to study the relationship between shadow bands with different eclipse geometries, we define two characteristic parameters. Let the angular radii of the sun and moon be R_S and R_M, respectively. Even though both of these radii may change from eclipse to eclipse, it is their ratio which defines the nature of the eclipse and has the greatest effect on shadow bands. Therefore, we define an "eclipse parameter," ε as

$$\varepsilon = \frac{R_M - R_S}{R_S} \tag{11}$$

The parameter ε is positive for total eclipses and negative for annular eclipses. A total eclipse where "Baily's beads" are prominent and seen over a large arc of the crescent will have an ε very near zero. A long total eclipse will have a larger value of ε than a shorter eclipse. We also define a normalized time parameter to describe changes within a given eclipse. Let Ω be the angular velocity of the moon relative to the sun. For an observer on the center of the path of totality, the normalized time away from totality is defined

$$\tau \equiv \frac{\Omega|t - t_{contact}|}{R_S} \tag{12}$$

where $t_{contact}$ is the time of either second or third contact (i.e. the beginning or end of totality), depending on whether we are in the waxing or waning phases of the eclipse. At both first and fourth contact (i.e. when the moon appears to just touch the sun's disk), τ has a value of two. At second or third contact, τ is zero. As a benchmark number, we will use 60 minutes for the interval from the beginning of the partial phase to totality. This gives approximate formulae for τ and ε in total eclipses as

$$\varepsilon \approx \frac{\text{duration of totality in minutes}}{60}$$

$$\tau \approx \frac{\text{time away from totality in minutes}}{30}$$

Typical values for ε are between 0 to 0.12 for total eclipses. Shadow bands are usually seen for times less than two minutes away from totality. Therefore, we are interested in values of τ between 0 and about 0.1.

A set of solar crescents is shown in Fig. 2. The geometry at a given instant is defined in Fig. 3. The most striking difference between eclipses with different values of ε is the extent of the crescent's horns. Treating the moon and sun as circles whose centers are separated by an angle $R_S(\varepsilon + \tau)$ we write the horn angles from the center of the moon and the sun as

$$\cos(\phi_M) = \frac{(1+\varepsilon)^2 + (\varepsilon+\tau)^2 - 1}{2(\varepsilon+\tau)(1+\varepsilon)}$$

$$\cos(\phi_S) = \frac{(1+\varepsilon)^2 - (\varepsilon+\tau)^2 - 1}{2(\varepsilon+\tau)}$$

Figure 4 shows the temporal evolution of the solar horn angle for various values of the eclipse parameter. Eclipses with smaller values of ε tend to keep their horns for a longer period of time while eclipses with larger values of ε lose their horns rapidly and display a lengthy "Diamond Ring" effect. Smaller horns mean

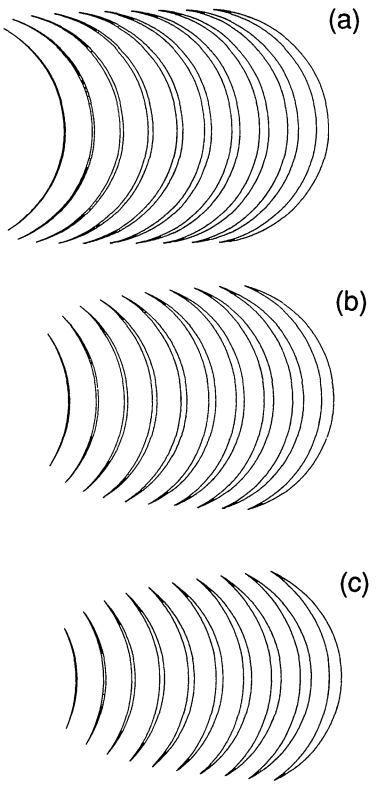

Fig. 2a–c. Evolution of solar crescents for an observer on the center of the path of totality. Crescents are shown at τ intervals of 0.01 and ε is (a) 0.01, (b) 0.05, and (c) 0.10

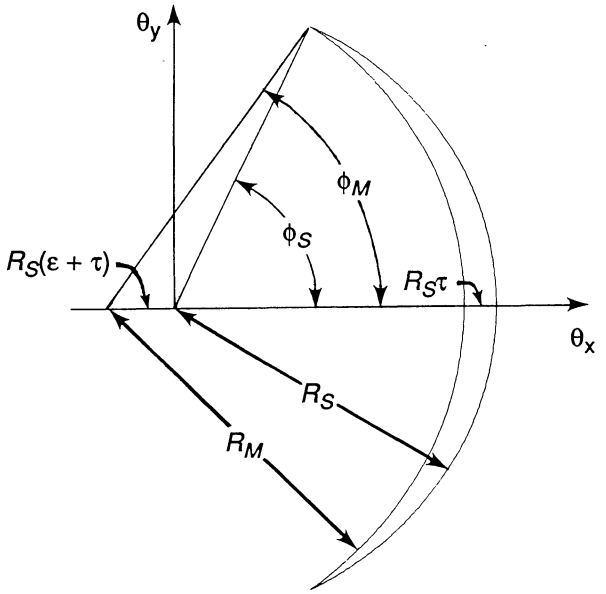

Fig. 3. Definitions of crescent angles and lengths

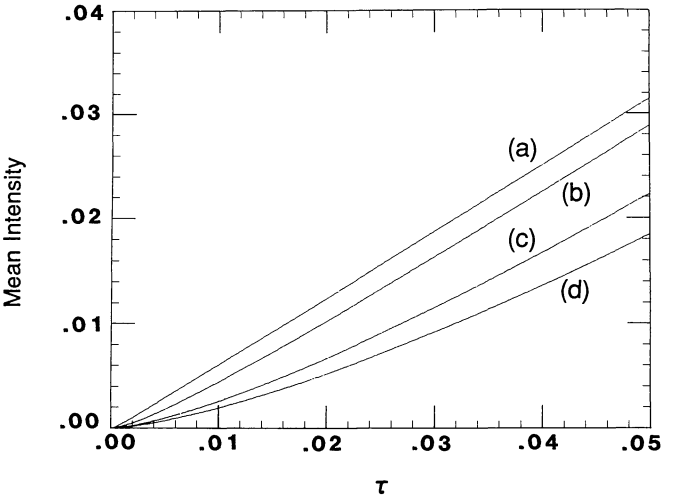

Fig. 5. Mean intensity of the solar crescent normalized to the full disk intensity for ε = (a) 0.001, (b) 0.01, (c) 0.05, and (d) 0.1

that the solar crescent is forming a better "slit." Thus, we expect eclipses with larger values of ε to make crisper shadow bands.

We also need to consider the mean intensity of the solar crescent. The mean intensity is used to normalize the intensity variance and plays an important role in the contrast of shadow bands. For simplicity, solar limb darkening will be ignored. Relative to the sun's full disk intensity the crescent's intensity is

$$\frac{I_{total}(\varepsilon,\tau)}{\pi R_S^2 B_0} = \frac{1}{2\pi}(2\phi_S - \sin(2\phi_S)) - \frac{1}{2\pi}(2\phi_M - \sin(2\phi_M)) \qquad (13)$$

where B_0 is the brightness of the solar disk. This normalized intensity is shown in Fig. 5 for several values of ε. The larger horns in small ε eclipses keep the intensity up much higher than in eclipses with a larger value of ε.

For an observer on the center of the path of totality, ε and τ completely specify the shape of the crescent (the crescent's orientation being a separate consideration). However, if the observer is not on the center of the path of totality, the crescent's orientation will be a function of time (Fig. 6) and the shape of the crescent will depend on the distance from the center-line as well as the time away from totality. The center of the crescent lies along the line joining the apparent centers of the sun and moon. For an observer off the center-line, the rotating crescent may still be described using two parameters: ε, which is unchanged, and an effective value of τ, corrected to account for the observer's position. The corrected value of τ is the normalized time at which an observer on the center-line would see the same shape for the crescent, ignoring rotation. The modified "time away from

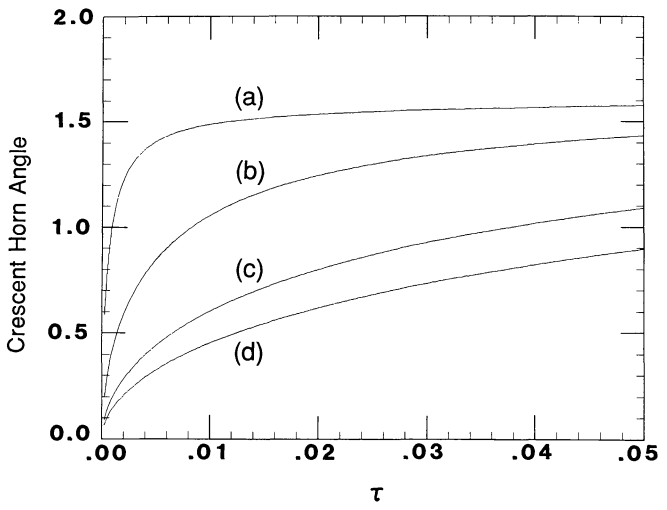

Fig. 4. Evolution of cresent horn angles for ε = (a) 0.001, (b) 0.001, (c) 0.005, and (d) 0.1

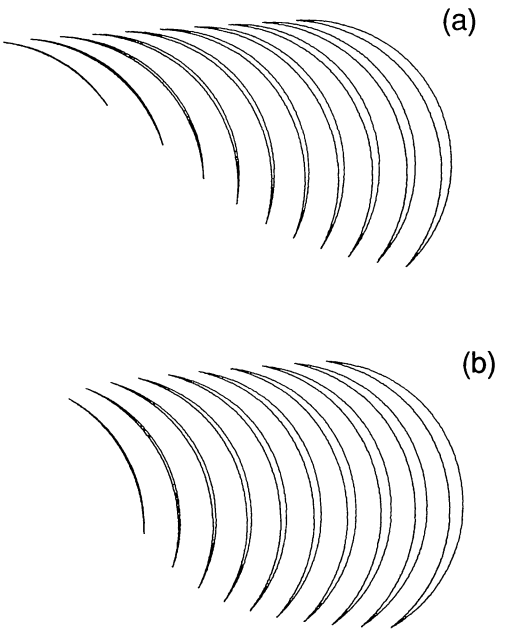

Fig. 6a and b. Evolution of the solar crescent for an observer not on the center of the path of totality. Crescents are shown at τ intervals of 0.01 for ε = 0.05 amd (a) ρ = 0.9, and (b) ρ = 0.5

totality" is defined

$$\tau = \begin{cases} (\tau_0^2 + 2\varepsilon\tau_0\sqrt{1-\rho^2} + \varepsilon^2)^{1/2} - \varepsilon & 0 \le \rho \le 1 \\ (\tau_0^2 + \rho^2\varepsilon^2)^{1/2} - \varepsilon & \rho > 1 \end{cases} \quad (14)$$

where τ_0 is the local normalized time away from totality found by using Eq. (12) and ρ is a normalized "impact parameter" describing the fractional distance of the observer from the centerline toward the edge of the path of totality. If $\rho > 1$, the observer will not experience totality at all. In that case, τ_0 is calculated using Eq. (12) with $t_{contact}$ replaced with the time of greatest partial phase. Note that for $\rho > 1$, τ never goes to zero (Fig. 7).

4. Shadow band intensity variance due to a phase screen

Calculation of the intensity spectrum requires knowledge of the power spectrum of the crescent's brightness distribution, $|\tilde{B}(z\boldsymbol{\kappa})|^2$. This is very difficult to calculate exactly. Fortunately, we can make two good approximations to $|\tilde{B}(z\boldsymbol{\kappa})|^2$: one that is valid for large values of $z\boldsymbol{\kappa}$ and one that is useful for small values of $z\boldsymbol{\kappa}$. Ignoring the effects of solar limb darkening, we write the brightness distribution as

$$B(\boldsymbol{\Theta}) = \begin{cases} B_0 & \text{if } \boldsymbol{\Theta} \text{ is inside the crescent} \\ 0 & \text{otherwise} \end{cases}$$

The corresponding source angular spectrum is

$$\tilde{B}(z\boldsymbol{\kappa}) = \frac{1}{(2\pi)^2}\int_{-\infty}^{\infty} B(\boldsymbol{\Theta}) e^{-iz\boldsymbol{\kappa}\cdot\boldsymbol{\Theta}} d^2\Theta = \frac{B_0}{(2\pi)^2}\int_C e^{-iz\boldsymbol{\kappa}\cdot\boldsymbol{\Theta}} d^2\Theta$$

where the area of integration C is the crescent. Using a two dimensional form of the divergence theorem we arrive at

$$\tilde{B}(z\boldsymbol{\kappa}) = \frac{iB_0}{(2\pi)^2 z\kappa^2}\int_{\partial C} \hat{n}(\boldsymbol{\Theta})\cdot\boldsymbol{\kappa} e^{-iz\boldsymbol{\kappa}\cdot\boldsymbol{\Theta}} d\Theta \quad (15)$$

where ∂C denotes the boundary of the crescent, $\hat{n}(\boldsymbol{\Theta})$ is the unit outward-facing normal, and $d\Theta$ is the differential angular path length along the edge of the crescent. Equation (15) lends itself to asymptotic analysis as $z\kappa R_S$ becomes large. Using the method of stationary phase and the fact that $\varepsilon^2 \ll 1$ we can write

$$|\tilde{B}(z\boldsymbol{\kappa})|^2 \approx \frac{8\pi B_0^2 R_S^4 (1+\varepsilon)^{1/2}}{(2\pi)^4 (z\kappa R_S)^3} \sin^2\left[\frac{z\kappa R_S}{2}(\varepsilon - (\varepsilon+\tau)\cos(\Psi))\right] \quad (16)$$

$$\text{for } z\kappa R_S \gg 1 \text{ and } |\Psi| < \phi_M$$

where Ψ is the angle between $\boldsymbol{\kappa}$ and Θ_x axis (Fig. 3). For $\Psi > \phi_S$, $|\tilde{B}(z\boldsymbol{\kappa})|^2$ is essentially zero. The region $\phi_S < \Psi < \phi_M$ has a different asymptotic behavior but may be neglected in practice. When we use Eq. (16) in Eq. (10) to find the scintillation index, we will be integrating over $\boldsymbol{\kappa}$ and hence Ψ. If $\phi_S < \frac{\pi}{2}$, the result of this integration is given asymptotically as

$$\int_0^{2\pi} |\tilde{B}(z\boldsymbol{\kappa})|^2 d\Psi \approx \frac{16\pi B_0^2 R_S^4 (1+\varepsilon)^{1/2}}{(2\pi)^4 (z\kappa R_S)^3}\left[\phi_S - \frac{\cos\left(z\kappa R_S\tau + \frac{\pi}{4}\right)}{\left(\frac{2}{\pi}z\kappa R_S(\varepsilon+\tau)\right)^{1/2}}\right] \quad (17)$$

for $z\kappa R_S \gg 1$. Note that the restriction on the horn angle excludes annular eclipses. An approximate form for the crescent's power spectrum along the $\Psi = 0$ axis is given by

$$|\tilde{B}(z\boldsymbol{\kappa})|^2 \approx \frac{I_{total}^2(\varepsilon,\tau)}{(2\pi)^4}\exp\left\{a_3\left(\exp\left\{\frac{-a_2u^2 + a_1u}{a_3}\right\} - 1\right) - a_1u\right\} \quad (18)$$

where

$$u = z\kappa R_S\tau$$
$$a_1 = 0.9$$
$$a_2 = \exp\{0.027\ln^2(\varepsilon+\tau) - 1.78\ln(\varepsilon+\tau) - 2.63\}$$
$$a_3 = 3\exp\{-11.0(\varepsilon+\tau)\}$$

Equation (18) is the result of numerical curve fitting and is good for $z\kappa R_S\tau$ between zero and about 3 or 4. Together, Eqs. (16) and (18) form an approximation for the source's angular power spectrum covering the entire range of κ for $\Psi = 0$ (Fig. 8). Using the symmetry of $|\tilde{B}(z\boldsymbol{\kappa})|^2$, integration over Ψ will be approximated by multiplying Eq. (18) by the factor $4\phi_S$.

We now have all of the information necessary to calculate the scintillation index due to a thin screen. We need only to pick the wavelength, λ, the distance to the screen, z, the strength of turbulence, C_n^2, and the parameters ε and τ. To see which altitudes are most efficient at generating intensity fluctuations, we define a "scintillation efficiency"

$$\eta_{m^2}(z,\lambda,\varepsilon,\tau) \equiv \frac{m^2}{lC_n^2} \quad (19)$$

where m^2 is the result of integrating Eq. (10). Larger values of η_{m^2} imply that more intensity variance will be generated for a given level of turbulence. Figure 9 shows η_{m^2} vs. z for different values of λ, ε, and τ. For larger values of z, the source's angular power spectrum limits the integral in Eq. (10). This "source averaging" reduces the scintillations by smearing the pattern on the ground. When the apparent width of the source is much

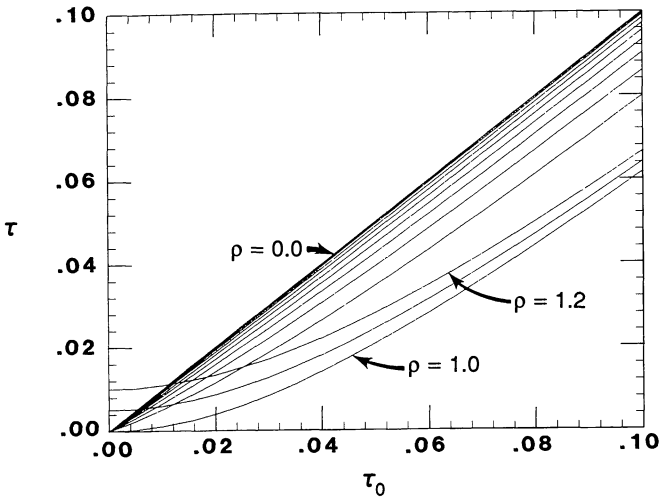

Fig. 7. An example demonstrating the relationship between the actual, normalized time to totality, τ_0, and the geometrical τ. The case shown is for $\varepsilon = 0.05$ and $\rho = 0$ to 1.2 at intervals of 0.1. Note that τ never goes to zero for $\rho > 1.0$

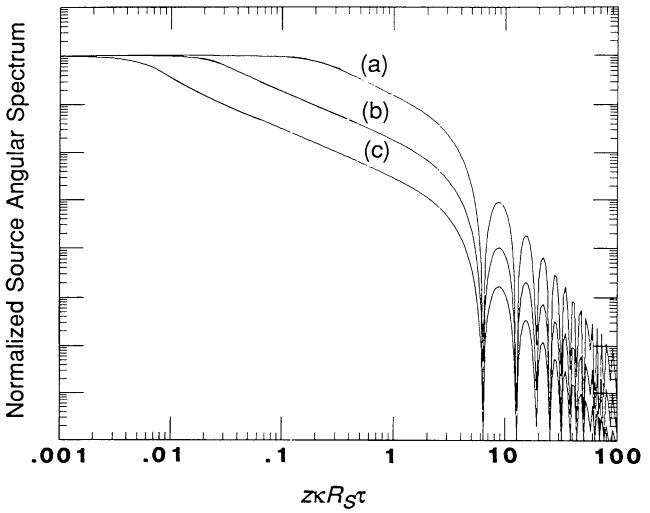

Fig. 8. A slice through the Fourier transform of the crescent's brightness distribution along the κ_x axis for $\varepsilon + \tau =$ (a) 0.1, (b) 0.01, and (c) 0.001

broader than $\sqrt{\lambda/z}$, the sine-squared factor may be approximated as $(z\kappa^2/2k)^2$, providing a factor which cancels the k^2 in front of the integral. Therefore, when the turbulence is sufficiently distant from the observer or the source sufficiently broad, the scintillations will be wavelength independent. At lower altitudes, the source does not provide a cutoff and the Fresnel filter will cause the intensity variance to be greater for shorter wavelengths. The transition altitude between wavelength-dependent and wavelength-independent scintillations depends on the width of the crescent and is proportional to λ/τ^2.

The eclipse parameter, ε, also has an effect on the scintillation efficiency. While not as important as source averaging, a smaller value of ε will degrade the scintillation efficiency at all altitudes. For two eclipses with identical viewing situations and weather, an eclipse with $\varepsilon = 0.01$ will have rms intensity fluctuations that are 20% less than an eclipse with $\varepsilon = 0.10$. Because shadow bands are usually near the limit of the eye's ability to detect contrast, and eclipses with smaller values of ε are brighter, the ε dependence could mean the difference between whether the bands are seen or not.

5. Phase screen shadow band structure

Features of shadow bands such as their orientation, spacing, motion, and linearity can all be discussed in terms of the intensity spectrum, Eq. (9). This spectrum is an ensemble average of the instantaneous spatial spectra and is ergodically related to a spatial average, *not* a temporal average. Since the spectrum evolves very rapidly near totality, temporal statistics are at best confused and at worst meaningless. For this reason, we will study the evolving morphology of the bands as snap-shot realizations of the spatial spectrum calculated for the appropriate time.

The orientation of the bands is controlled by the orientation of the crescent, which is a function of time for an observer not on the center of the path of totality. In other words, the crescent's angular power spectrum, $|\tilde{B}(z\kappa)|^2$, rotates with the crescent, and since $|\tilde{B}(z\kappa)|^2$ is the only source of anisotropy in $\Phi_I(\kappa)$, the shadow bands will also rotate. A possible caveat is that there may be some horizontal anisotropy in the turbulence spectrum not included in

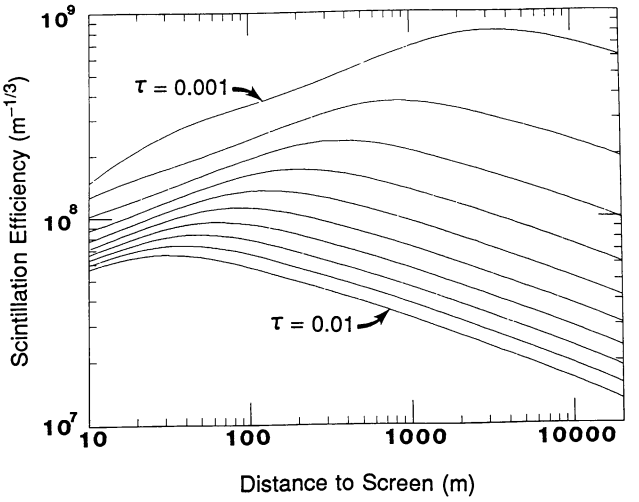

Fig. 9a. The evolution of the scintillation efficiency profile vs. τ plotted against distance from the observer. The case shown is for $\varepsilon = 0.05$ and $\lambda = 6000$ Å

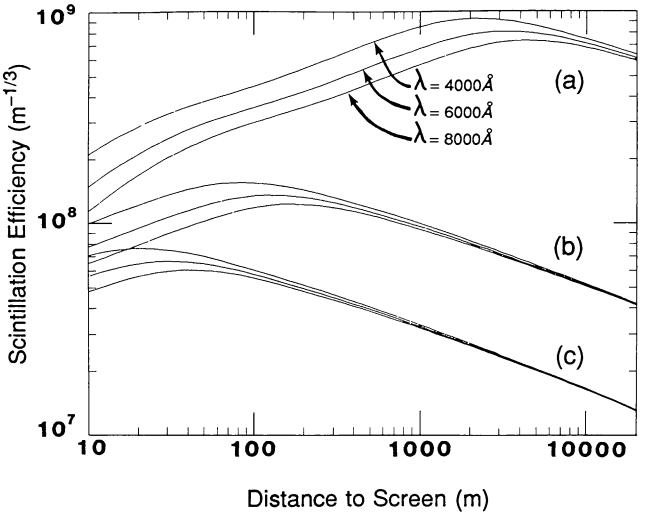

Fig. 9b. The effect of changing the wavelength on the scintillation efficiency profile for $\varepsilon = 0.05$ and $\tau =$ (a) 0.001, (b) 0.005, and (c) 0.01

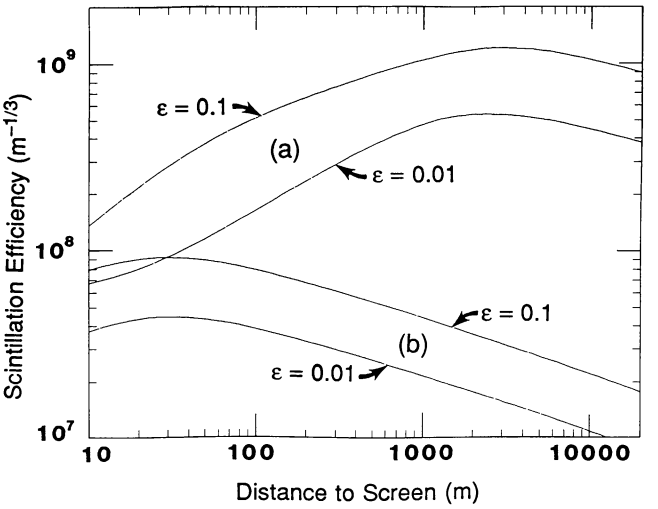

Fig. 9c. The scintillation efficiency profile for two different values of ε at two different times, $\tau =$ (a) 0.001 and (b) 0.01

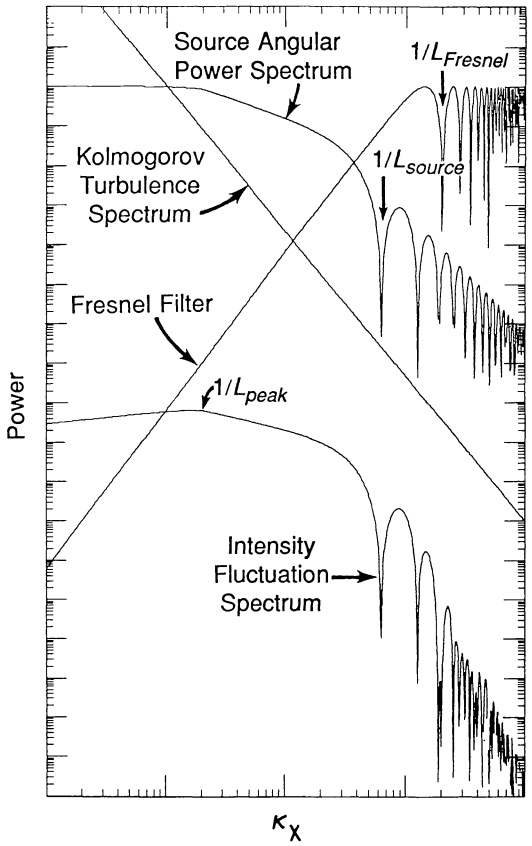

Fig. 10. Plot of the shadow band intensity fluctuation spectrum perpendicular to the solar crescent showing the three major scales. The component factors that comprise the spectrum are also shown

the standard Kolmogorov turbulence model. Such an anisotropy might be due to atmospheric gravity waves propagating through the background turbulence. However, since photographs of the scattered light from stars appear isotropic, the medium's anisotropy is unlikely to be an important effect.

In our phase screen model, the intensity pattern on the ground will move if the screen is moved perpendicular to the line of sight. Therefore, wind convecting turbulent eddies through the atmosphere (Taylor's hypothesis of convected "frozen" turbulence) simply shifts the intensity pattern on the ground. However, the turbulent eddies are themselves rearranging in time. Furthermore, atmospheric turbulence is not confined to a thin layer and the mean wind is a function of altitude. Each of these latter effects cause further time dependence in the intensity pattern and a reduction of the spatial correlation of intensity on the ground. When the intensity pattern has a large axial ratio, only the wind component perpendicular to the bands will be evident in the observed motion. If the wind is parallel with the bands, they may be very difficult to see even if the intensity fluctuations are relatively strong. Under such circumstances, the dominant time dependence would be due to turbulent rearrangement, leading to a "shimmering" effect that might not catch the eye as well as moving bands. The combination of this effect with the changing orientation of the crescent could explain why shadow bands are sometimes seen on one side of totality but not the other. Annular eclipses and eclipses with small values of ε have much less ansotropy in $|\tilde{B}(z\kappa)|^2$, so that the wind has a much higher probability of blowing in a direction effectively parallel to the crescent. This is another reason why small ε eclipses are not likely to generate profound shadow band events.

The intensity spectrum can be discussed in terms of characteristic length scales. The characteristic length scale parallel to the bands is controlled by the height of the turbulent layer as well as the geometry of the crescent and has a value of roughly $L_{parallel} \equiv zR_S \sin(\phi_S)$. The characteristic length scale perpendicular to the bands is not as straightforward to calculate. The intensity spectrum perpendicular to the crescent for a screen at a given altitude has three characteristic scales (Fig. 10). The largest scale is controlled by the geometry of the crescent and is

$$L_{peak} \approx 2\pi z R_S \tau \sqrt{6a_2(\varepsilon, \tau)} \tag{20}$$

corresponding to the low spatial-frequency peak in the spectrum. The parameter $a_2(\varepsilon, \tau)$ is given in Eq. (18). The next scale is due to the first null of the source spectrum.

$$L_{source} = zR_S\tau \tag{21}$$

The third scale is the length corresponding to the first non-trivial zero of the Fresnel filter:

$$L_{Fresnel} = \sqrt{\lambda z} \tag{22}$$

Which of the above lengths will be the dominant shadow band scale will depend on the distance of the screen from the observer and the time to totality, τ.

The eye's response to moving intensity patterns is a strong function of the pattern's observed angular velocity (Kelly, 1979). Visual sensitivity also drops off precipitously at both low and high spatial frequencies. For common shadow band contrast levels of 2 to 3% the lowest visible spatial-frequency differs from the highest by less than a factor of 50, bandwidth decreasing with increasing pattern speed. This implies that if an observer can see scales on the order of a few centimeters, scales larger than 1 to 2 meters would be invisible. Therefore, even though there is a great deal more variance at L_{peak} than in the vicinity of L_{source} or $L_{Fresnel}$, these latter scales will be much more visible.

The only exception is when the screen is very near the observer, say 100 meters or less. In such a case the Fresnel filter and the source spectrum combine to form a high-pass spatial filter in one direction, causing an effect similar to a crude Schlieren camera. The effect would be to create intensity fluctuations on the ground that are like refractive "shadows" of the turbulent irregularities. These patterns would appear more like "smoky wisps" than shadow bands. The broad source in the direction parallel to the crescent limits the refractive resolution of the irregularities to $L_{parallel}$. Thus the "smoky wisps" would have a characteristic width L_{peak} and a longitudinal scale of roughly $L_{parallel}$. At longitudinal distances greater than $L_{parallel}$ the pattern would appear to lose linearity and wander randomly.

When the screen is 1000 meters or more away from the observer, the fluctuations with scale L_{peak} will be too large to see until very near totality. The scales of interest are now L_{source} and $L_{Fresnel}$. Two minutes away from totality, a screen at 1000 meters will have a value of L_{source} of about 30 cm, decreasing linearly with τ as totality nears, and a Fresnel length scale of about 2.5 cm. As L_{source} drops toward $L_{Fresnel}$, the power in the intensity spectrum will increase in the vicinity of $1/L_{Fresnel}$ and the intensity pattern will develop structures with characteristic scale $L_{Fresnel}$. Finally, when L_{source} is smaller than $L_{Fresnel}$, the larger scale will remain dominant. Whenever structures at the Fresnel scale are

visible, the band spacing will be wavelength dependent since $L_{Fresnel} \propto \sqrt{\lambda}$. Moreover, the intensity variance in the pattern will be greater with smaller wavelength. From the time when $L_{source} \approx L_{Fresnel}$ to totality, the pattern will remain wavelength dependent with scale $L_{Fresnel}$ while the contrast continues to increase. In the last few moments before totality, L_{peak} will drop into the visible range and provide some larger scale contrast patterns superimposed on the smaller, wavelength dependent shadow bands.

A screen at an altitude of 10 km would have the same behavior as given above except the source averaging will keep the pattern's contrast low until relatively near totality. For a screen at an altitude of 10 km, it is only within a few seconds of totality that sufficient scintillation power is present to make the patterns visible.

How well the shadow bands display wavelength-dependent structures depends on ε. While the high spatial-frequency asymptotic form of $|\tilde{B}(z\boldsymbol{\kappa})|^2$ depends only weakly on ε, the total intensity, I_{total}, depends strongly on ε. Since I_{total} is much larger for small ε eclipses, the *relative contrast* in the asymptotic region will be smaller. This means that eclipses with larger values of ε will be better at producing the narrow, wavelength-dependent, high axial-ratio patterns usually associated with shadow bands. The relative power in the intensity spectrum for $\kappa \approx 1/L_{peak}$ is much less sensitive to the total intensity of the crescent. Consequently, small ε eclipses would still display the features associated with L_{peak}. Furthermore, since L_{peak} effects are only visible when the screen is close to the observer, we expect that small ε eclipses or annular eclipses will predominantly display the random, smoky patterns caused by low level Schlieren effects.

The last point to consider is how a time series of intensity is related to our calculations. Unfortunately, shadow band time series are very complicated and an accurate analysis requires a great deal of information. The simplest approach is to assume that the turbulence is "frozen" and does not rearrange as it is transported by the wind (Taylor's hypothesis). The velocity of the intensity pattern is then equal to the component of the wind perpendicular to the line of sight $\boldsymbol{v}$. For the moment we will ignore the fact that the crescent is changing rapidly in time. Using Taylor's hypothesis we see that

$$I(\boldsymbol{x}, t_0) = I(\boldsymbol{x} - \boldsymbol{v}t, t_0 + t)$$

which leads us to the temporal intensity correlation as

$$C_{I,temporal}(t) = C_I(\boldsymbol{v}t) \tag{23}$$

Transforming (23) with respect to t produces the temporal intensity power spectrum

$$\Phi_{I,temporal}(f) = \frac{2\pi}{v} \int_{-\infty}^{\infty} \Phi_I\left(\kappa_\perp, \kappa_{||} = \frac{2\pi f}{v}\right) d\kappa_\perp \tag{24}$$

where $\kappa_{||}$ and $\kappa_\perp$ are the components of $\boldsymbol{\kappa}$ parallel and perpendicular to the wind vector, $\boldsymbol{v}$, and f is the temporal frequency in cycles per second. We may include the effect of the finite detector aperture by multiplying the right hand side of Eq. (9) by $(2\pi)^4|\tilde{A}(\boldsymbol{\kappa})|^2$ where $\tilde{A}(\boldsymbol{\kappa})$ is the Fourier transform of the detector's aperture distribution. The difficulty in the analysis comes from the fact that the wind vector typically lies along some direction other than the perpendicular to the crescent; leading to a rather complicated integral. However, the "strip integration" in Eq. (24) washes out most of the oscillatory structure in the source's angular power spectrum and the Fresnel filter allowing us to find approximate scaling laws for the temporal intensity spectrum. For a detector aperture of size $L_{aperture}$, we would expect to see no power for temporal frequencies greater than about $v/L_{aperture}$. If $v/L_{Fresnel} \ll f \ll v/L_{aperture}$ and the apparent wind is at angle less than $\frac{\pi}{2} - \phi_S$ to the Θ_x axis, the temporal intensity spectrum will scale approximately as $f^{-17/3}$. In the frequency range $v/L_{source} \ll f \ll v/L_{Fresnel}$ the scaling will be roughly $f^{-5/3}$. For $f \ll v/L_{source}$ or when $L_{Fresnel} > L_{source}$, the spectrum will depend strongly on the details of the source's angular power spectrum and the wind direction. If the apparent wind is at an angle greater than $\frac{\pi}{2} - \phi_S$, the lower temporal frequencies will be greatly enhanced. For this case, the analysis of the temporal spectrum's shape would require detailed numerical calculations specific to the observation geometry and the wind direction.

The inherent difficulties in shadow band time series analysis are compounded by the dynamic character of the crescent's brightness distribution. Estimates of the temporal intensity spectrum must be derived from sufficiently short time series so that the crescent may be considered unchanging. From this perspective it may be preferred to examine time series taken relatively far from totality. Unfortunately, this does not permit making use of the stronger fluctuations near totality. The other option would be to use shorter time series. However, this approach would lead to prohibitive spectral estimation error unless the wind speed was quite high.

6. The effects of extended atmospheric turbulence

Atmospheric turbulence is not confined to a thin layer. It is present everywhere from the ground to tens of kilometers in altitude. The scintillation efficiency of a star is never limited by its brightness distribution. It is given by

$$\eta_{m^2,star} = 2.2k^{7/6}z^{5/6}$$

which increases monotonically with z. Because distant turbulence is more effective than nearby turbulence, stellar scintillations are commonly said to be primarily due to turbulence in the tropopause at an altitude of 10–12 km. However, lower altitude turbulence, which is more responsible for the related phenomenon of "seeing," can contribute substantially to a star's scintillations. Young (1969) noted that planetary scintillation intensity spectra could not be well modeled by considering only a thin screen at the tropopause. A finite-diameter source may be more sensitive to high-level or low-level turbulence depending on the scintillation efficiency profile. Shadow bands are unique in that their scintillation efficiency evolves rapidly and dramatically with time. For larger values of τ, shadow bands are more sensitive to turbulence near the ground. As totality nears, turbulence at higher altitudes plays an increasingly more important role. This will change the shadow bands' wavelength dependence as well as their morphology as time progresses.

The models described in the previous sections can be modified to take extended turbulence into account. As long as the scattering is weak, the intensity fluctuation spectrum is the linear superposition of the thin screen results. If the sun is *not* at the zenith, the altitude is given by $z\cos(\zeta)$ where ζ is the sun's zenith

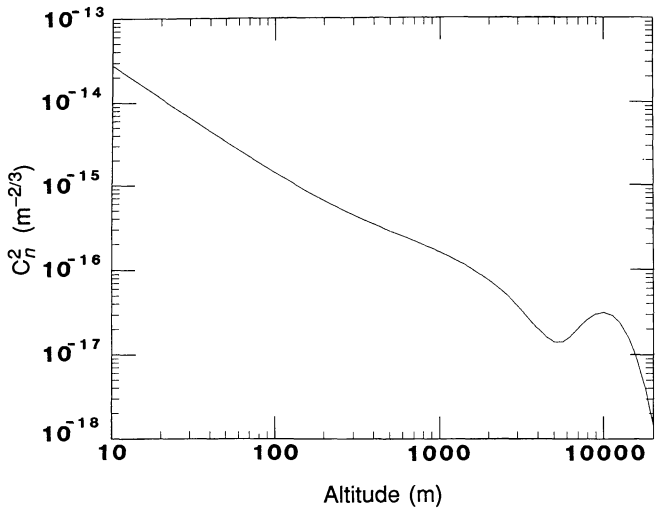

Fig. 11. Plot of the modified Hufnagel turbulence profile

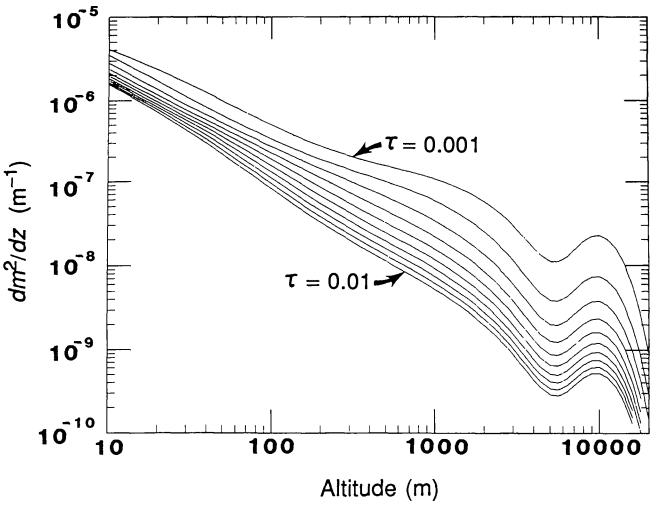

Fig. 12a Evolution of the scintillation index profile for $\lambda = 6000$ Å, $\varepsilon = 0.05$, and τ at intervals of 0.001 from 0.001 to 0.01

angle. The resulting formula for the intensity spectrum becomes

$$\Phi_I(\boldsymbol{\kappa}) = I_{total}^2\,\delta(\boldsymbol{\kappa}) + (2\pi)^5(0.132)\kappa^{-\alpha}\int_0^\infty |\tilde{B}(z\boldsymbol{\kappa})|^2 C_n^2(z\cos(\zeta))\sin^2\left(\frac{z\kappa^2}{2k}\right)dz \tag{25}$$

where $C_n^2(h)$ is the turbulence structure constant at altitude h. Combining Eqs. (25), (19), and (10) gives the total scintillation index as

$$m^2(\lambda,\varepsilon,\tau,\zeta) = \int_0^\infty C_n^2(z\cos(\zeta))\eta_{m^2}(z,\lambda,\varepsilon,\tau)\,dz \tag{26}$$

The integrand in Eq. (26) shows the relative importance of each distance to the total intensity fluctuation spectrum. Given the turbulence strength profile, $C_n^2(h)$, we can see which altitudes are contributing most to the shadow bands. $C_n^2(h)$ is known to vary with time of day, season, geographical position, humidity, wind speed, and surface texture (Fante, 1980). For our purposes, we will use a combination of models to generate a generic turbulence profile. Our profile will be a form of the Hufnagel model (Hufnagel, 1974), modified to account for the strong turbulence at low altitudes, given by

$$C_n^2(h) \approx C_n^2(1)h^{-4/3}e^{-h/1000} + (2.7\times10^{-16})e^{-h/1500} + (8.1\times10^{-16})\langle v^2\rangle\left(\frac{h}{10000}\right)^{10}e^{-h/1000} \tag{27}$$

where h is the altitude in meters, $C_n^2(1)$ is the turbulence structure constant at 1 meter, and $\langle v^2\rangle$ is the mean-square wind speed at high altitudes. For the calculations that follow, we assume "typical" values for the constants in (27): $C_n^2(1) \approx 6\times10^{-13}\,m^{-2/3}$ and $\langle v^2\rangle \approx 850\,m^2/s^2$. The resulting turbulence profile is shown in Fig. 11. The peak at 10000 m is the enhanced turbulence at the tropopause.

The resulting contribution to the total scintillation index for various altitudes is shown in Fig. 12. Figure 12a shows the temporal evolution of the m^2 profile for a typical eclipse. At about two minutes before totality, only turbulence very near the ground is making substantial contributions to be intensity fluctuations.

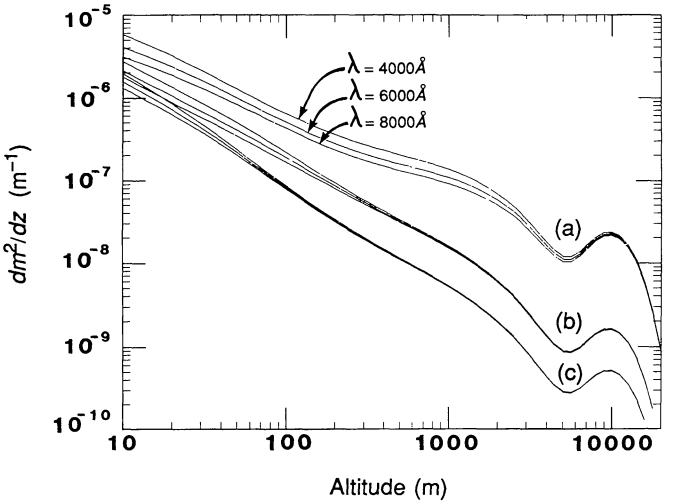

Fig. 12b. The effect on the scintillation index profile of changing the wavelength for $\varepsilon = 0.05$, and τ = (a) 0.001, (b) 0.005, and (c) 0.01

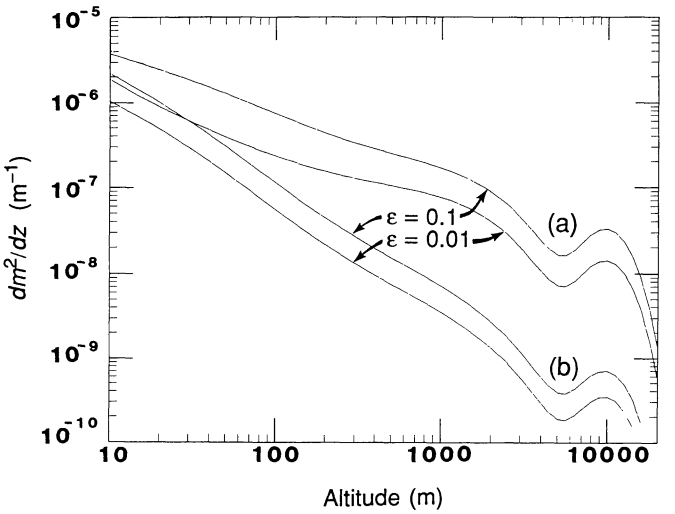

Fig. 12c. The effect on the scintillation index profile of changing the eclipse parameter ε for τ = (a) 0.001 and (b) 0.01

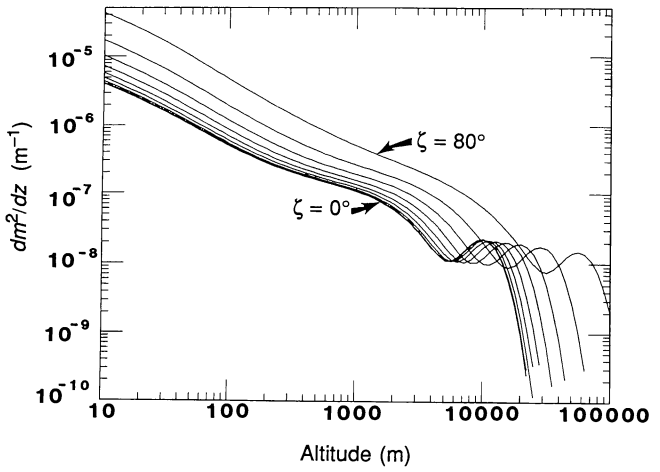

Fig. 12d. The effect on the scintillation index profile of changing the zenith angle, ζ, for $\tau = 0.001$ and $\lambda = 6000$ Å. Note that the scintillation index increases as well as the scattering distance

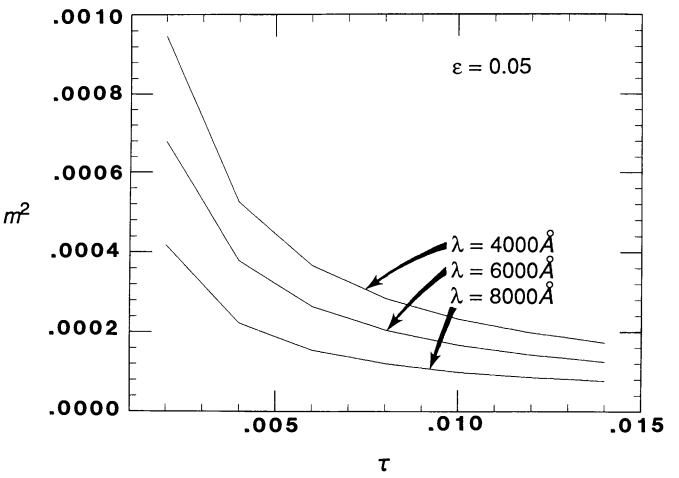

Fig. 13. Evolution of the total scintillation index for $\varepsilon = 0.05$ and $\lambda =$ 4000, 6000, and 8000 Å

Even by 20 seconds before totality, the turbulence within the bottom two kilometers is responsible for essentially all of the scintillations. Only within 5 to 10 seconds of totality does the high altitude turbulence make a noticeable effect. However, even at this late time, the turbulence within two kilometers of the ground is much more important than the turbulence at the tropopause. Figure 12b shows the dependence of the scintillation profile on wavelength. At twenty seconds before totality, the wavelength dependence is confined to within a few hundred meters of the ground. By ten seconds away from totality, the wavelength dependence has spread to include all of the lower altitude turbulence while the scintillations from the tropopause are still wavelength independent. Only within a few seconds of totality does the tropopause produce wavelength-dependent scintillations. Figure 12c shows that the scintillation contribution is degraded at all altitudes equally for smaller ε eclipses. Figure 12d shows the effect of zenith angle on the scintillation profile. Note that not only are the scintillations stronger, they are the result of the more distant turbulence.

The total scintillation index for a typical eclipse is shown in Fig. 13. An observer's estimate of the intensity variance would depend on the scales observed. The calculations shown in figure 13 include *all* scales. As long as the turbulence in the bottom few kilometers dominates the scintillations, we may treat C_n^2 as being proportional to $h^{-4/3}$. This leads to the approximate scaling formula for m^2 with zenith angle:

$$m^2(\zeta) = (\sec(\zeta))^{4/3} m^2(\zeta = 0) \tag{28}$$

The m^2 profile allows us to define a "typical" scattering distance, $\bar{z}$, which is the centroid of the scintillation contributions, written

$$\bar{z} = \frac{\int_0^\infty z C_n^2(z\cos(\zeta))\eta_{m^2}(z)\,dz}{\int_0^\infty C_n^2(z\cos(\zeta))\eta_{m^2}(z)\,dz} \tag{29}$$

A more meaningful estimate of the typical scattering distance is achieved by treating the low alitude and the tropopause turbulence contributions separately. In our turbulence profile model, Eq. (27), the tropopause turbulence is described by the last term. Calculating the moments of these terms separately, two typical scattering distances are found (Fig. 14). Note that the typical

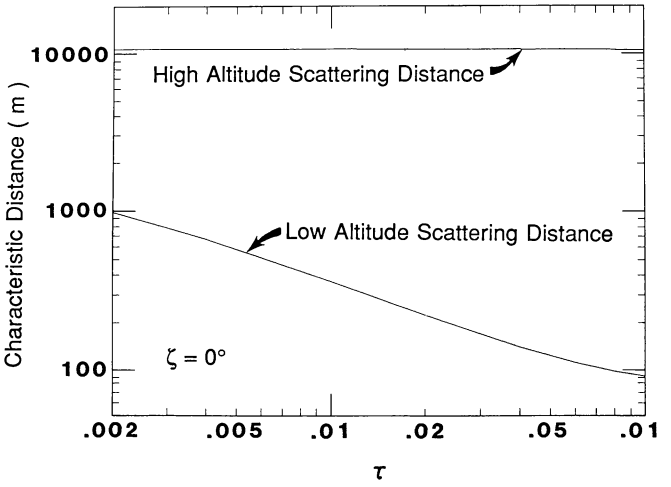

Fig. 14a. Typical scattering distances vs. time at the zenith. The eclipse parameter, ε, is 0.05

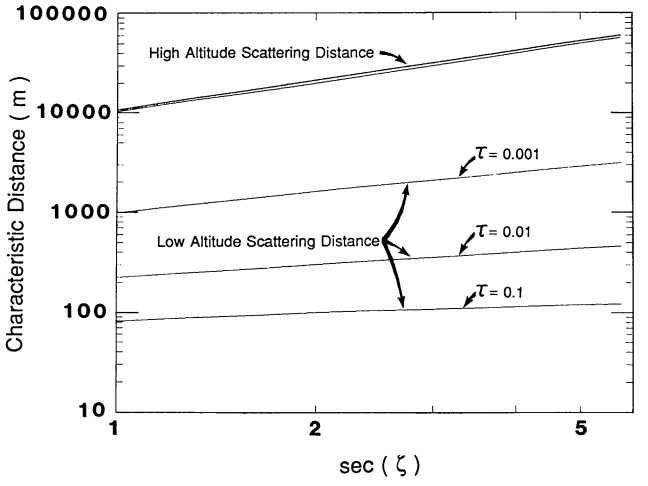

Fig. 14b. Typical scattering distances vs. zenith angle. The eclipse parameter, ε, is 0.05

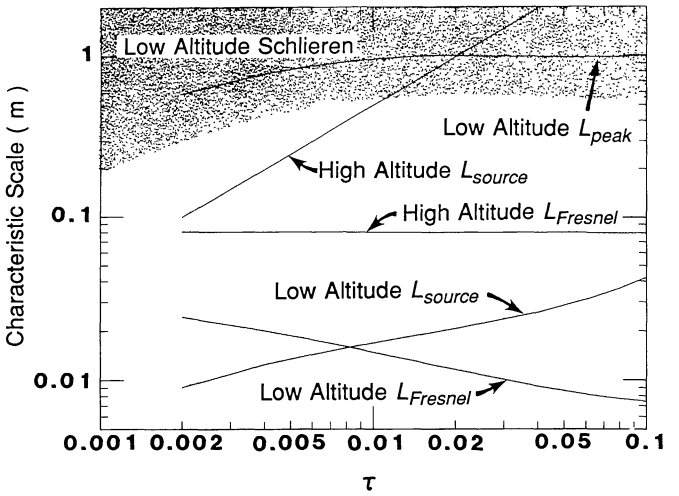

Fig. 15. Evolution of the characteristic scales vs. time. The case shown is for $\varepsilon = 0.05$ and $\zeta = 0$

scattering distance of the low-altitude turbulence is rather insensitive to zenith angle while the tropopause distance increases with ζ.

The structure of shadow bands in the extended turbulence model is a combination of thin screen model structures from all of the contributing distances. A good picture of the evolving scales may be found, without making a detailed spectrum calculation, by using the thin screen model appropriate for the typical scattering distance. The structure is found by using Eqs. (20), (21), and (22) with z replaced by $\bar{z}$. The effect of the actual, distributed turbulence will be to make the thin screen scales less distinct, rather than to introduce any new scales. The thin screen scales are shown in Fig. 15. Features much larger than 1 meter are not visible and are not shown although they contribute to m^2. When the scintillations first become visible, they present primarily wavelength-independent structures with scale L_{peak} from turbulence very near the ground. As totality nears, the typical scattering distance goes up and the prominent scale becomes L_{source} from the low altitude turbulence. The intensity pattern will be somewhat wavelength-dependent due to the wavelength dependence of the typical scattering distance. The scintillations from the tropopause are still suffering from source averaging and are too faint to be seen. As the crescent narrows, the axial ratio of the pattern increases and the patterns become true "shadow bands." The very low pattern contrasts will lead to the observation that the bands are narrow dark strips separated by larger bright regions due to the logarithmic sensitivity of the eyes (Cornsweet, 1970). As the contrast increases, the pattern will appear to have roughly equal strips of light and dark. Finally, structures at scale L_{source} merge with structures at scale $L_{Fresnel}$ and the wavelength dependence becomes maximum. Once $L_{Fresnel}$ is the dominant scale, the pattern spacing will slowly increase as the typical scattering distance continues to increase. Meanwhile, scintillation structures with scale L_{peak} will have returned to a visible size, displaying small axial-ratio patterns superimposed on the shadow bands. In the last few seconds from totality, the tropopause finally makes a visible contribution, with patterns at the tropopause's scale L_{source} rapidly merging with $L_{Fresnel}$. If the eclipse has a small value of ε, the axial ratio is never as great as in longer eclipses. In addition, the mean intensity is greater causing a diminished contrast at all scales except L_{peak}. Therefore, small ε eclipses and annular eclipses will predominantly generate the random, smoky patterns associated with L_{peak}.

Since the wind velocity is often a function of altitude, the shadow band motion may change as the typical scattering distance moves to greater altitudes. If a wind-shear layer is present, distinct shadow band patterns may be seen superimposed on each other, moving with different speeds. If the observer is not on the center of the path of totality, the band motion will be even more complex: the wind component perpendicular to the bands changing as the crescent rotates. Complications due to wind speed variations are yet another insurmountable problem in shadow band time series analysis. The most reasonable approach would be to treat the scintillations as if they arose from a thin screen located at the typical scattering distance and ignore changes in the shadow band speed during the observation. Nevertheless, the error analysis should seriously take such factors into account.

The generic turbulence profile, Eq. (27), has given us a perspective on the evolution of a typical shadow band event. However, the actual turbulence profile present at an observation site may differ greatly from the model. In addition to differences in the large-scale turbulence distribution, an actual C_n^2 profile is *not* smooth; it is layered and patchy (Bufton, et al., 1972). One general principle may be inferred from the generic profile: shadow band visibility is largely controlled by the level of turbulence within the bottom 2–3 kilometers of the atmosphere. Therefore, any situation in which the lower-altitude C_n^2 is diminished will degrade the shadow band display. Such cases would include sites with very good "seeing" or places with high humidity, such as near lakes or on the ocean. Sites where the eclipse is seen further from the zenith will tend to show stronger shadow bands. Observations made under very windy conditions should not make good visual shadow band events due to the response time of the eye. However, properly sampled photoelectric observations obtained under similar circumstances should still detect the intensity fluctuations and the higher frequencies would lead to better temporal spectrum estimates.

7. Summary and comparison with experiments

In the preceding sections, we have seen how weak scattering scintillation theory can be used to explain all of the salient features of eclipse shadow bands. The unknown turbulence and wind speed profiles are the only reasons why explicit shadow band predictions are not possible. However, with reasonable assumptions about the meteorology, many features of the shadow bands may be understood.

The band motion is driven by the wind component perpendicular to the bands at the various contributing altitudes. The band orientation is parallel with the solar crescent and is a function of time for an observer off the center of the path of totality. The bands will be perpendicular to the lunar shadow's path far from totality and parallel with the edge of the shadow near totality. The band spacing is a complicated interplay of three intensity spectrum scales and a changing scattering altitude. The patterns start out random and disorganized, becoming more linear and organized as the crescent narrows and the scattering height increases. The band spacing decreases as totality nears, becoming progressively more wavelength dependent with a final

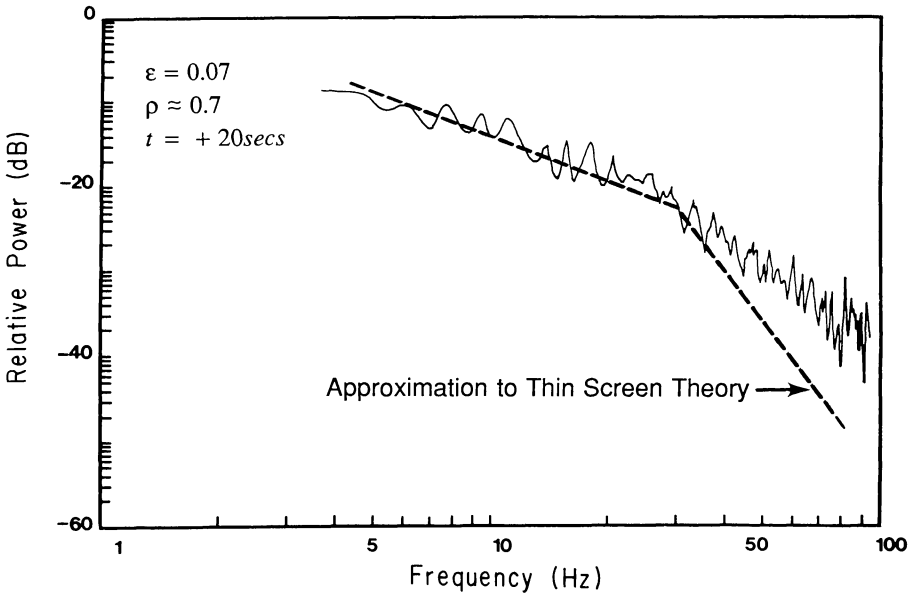

Fig. 16. Measured shadow band time series power spectrum (Marschall, 1984) compared to the approximate thin screen model. The bend in the model spectrum is at approximately $v/L_{Fresnel}$. The corresponding wind speed is roughly 1 m/s

spacing proportional to $\sqrt{\lambda}$. The pattern contrast becomes wavelength dependent as diffraction effects become more important near totality, shorter wavelengths exhibiting higher contrast patterns. Both pattern contrast and spacing increase with increasing zenith angle. The scintillation theory provides no means for polarization effects and none are expected. Shorter eclipses and annular eclipses are not efficient at generating high axial-ratio shadow bands; only random, smoky patterns from the turbulence near the ground. Shadow bands are related to the same turbulence responsible for "seeing:" good seeing implies poorer shadow band contrast. All shadow band phenomena are statistically symmetric before and after totality, except for motion. The temporal structure of the intensity fluctuations is strongly dependent on the direction and altitude distribution of the wind.

Several experimental studies of the shadow band phenomena have been performed. Unfortunately, published experiments with sufficient information and quality to make useful theoretical comparisons are rare. Three of the best are Hults, et al. (1971), Quann and Daly (1972), and Marschall, et al. (1984).

Hults et al. made a study of shadow band orientation within the path of totality. They noted a rotation of the bands when the observer was not on the center of the path of totality. Quann and Daly noted the same rotation and correctly attributed it to the apparent rotation of the solar crescent. Their position was just outside of the path of totality and, hence, they would have observed the solar crescent rotate by nearly 180°. They reported data from a rawinsonde, launched prior to the eclipse, which showed the wind to be roughly parallel with the path of totality. They also made a detailed photoelectric survey to study polarization and wavelength effects. They found no polarization effects and their aggregate power spectra had widths scaling roughly as $\sqrt{\lambda}$. Unfortunately, they apparently averaged *all* times into their spectra and more detailed conclusions may not be drawn. In the blue and ultraviolet, they observed the temporal frequency of the bands to drop with the bands becoming invisible near maximum partial eclipse. This was not seen in the green-yellow observations. During the time of this "cutoff," the wind was roughly parallel to the bands and the wavelengths affected would have had the greatest axial ratio. Additionally, the actual effect of solar limb darkening would be to reduce the mean intensity of the solar crescent in blue and ultraviolet near totality. Therefore, the observed cutoff may have been due to insufficient mean intensity at those wavelengths.

The best temporal intensity spectrum measurements to date were made by Marschall et al. (1984). Their two published spectra were taken sufficiently far from totality that the crescent's evolution could be ignored. The noise in the pre-totality spectrum appears more pronounced than in the post-totality spectrum, suggesting that the wind was more nearly perpendicular to the bands after totality. Assuming $v/L_{Fresnel}$ to be about 30 Hz (corresponding to a wind speed of roughly 1 m/s), the approximate scaling form of the temporal power spectrum may be compared to their post-totality spectrum (Fig. 16). The level of theoretical curve is set to approximate the lower frequency portion of the data. The thin screen spectrum is too steep above $v/L_{Fresnel}$. This is doubtless due to the distributed nature of the turbulence, lower altitudes providing higher frequency intensity fluctuations.

Despite the high quality of the power spectrum obtained by Marschall et al., the uncertainties involved in the time dependence and wind direction make an exact comparison with the theory difficult. Two-dimensional observations that did not depend on pattern drift would be far better. Perhaps with the advent of higher quality video cameras and photographic film, better comparisons will be possible in the future.

Acknowledgements. It is a pleasure to acknowledge Stanley Flatté and the La Jolla Institute, Center for Studies of Nonlinear Dynamics, for support and encouraging me to pursue this application of scintillation theory to the end. I would also like to thank Rod Frehlich for technical feedback, Bernie Jackson for enthusiasm, and Laurence Marschall for providing Fig. 16.

This work has been supported in part by the Defense Advanced Research Projects Administration (DARPA), independent research funds of the La Jolla Institute, and Air Force contract F19628-85-K-0037.

References

J.L. Bufton, P.O. Minott, M.W. Fitzmaurice, and P.J. Titterton, "Measurements of Turbulence Profiles in the Troposphere," *J. Opt. Soc. Am.* **62**, 1068 (1972).

T.N. Cornsweet, *Visual Perception*, (Academic Press Inc., New York, N.Y., 1970).

R.L. Fante, "Electromagnetic Beam Propagation in Turbulent Media: An Update," *Proc. IEEE* **68**, 1424 (1980).

R. Hufnagel, "Variations of atmosphere turbulence," in *Dig. Tech. Papers, Topical Meet. Optical Propagation Through Turbulence*, pp. Wa 1-1 to Wa 1-4 (Optical Society of America, Washington, DC, 1974).

M.E. Hults, R.D. Burgess, D.A. Mitchell, and D.W. Warn, "Visual, Photographic, and Photoelectric Detection of Shadow Bands at the March 7, 1970, Solar Eclipse," *Nature* **231**, 255 (1971).

D.H. Kelly, "Motion and vision. II. Stabilized spatio-temporal threshold surface," *J. Opt. Soc. Am.* **69**, 1340 (1979).

L.A. Marschall, "Shadow Bands—Solar Eclipse Phantoms," *Sky Telesc.* **67**, 116 (1984).

L.A. Marschall, R. Mahon, and R.C. Henry, "Observations of shadow bands at the total eclipse of 16 February 1980," *Appl. Opt.* **23**, 4390 (1984).

M. Minnaert, *The Nature of Light and Color in the Open Air* (Dover, New York, 1954).

J.J. Quann and C.J. Daly, "The Shadow Band Phenomena," *J. Atmos. Terr. Phys.* **34**, 577 (1972).

E.E. Salpeter, "Interplanetary Scintillations, 1, Theory," *Astrophys. J.* **147**, 443 (1967).

V.I. Tatarskii, *The Effects of the Turbulent Atmosphere on Wave Propagation* (National Technical Information Service, Springfield, VA., 1971).

A.T. Young, "Photometric Error Analysis. 8: The Temporal Power Spectrum of Scintillation," *Appl. Opt.* **8**, 869 (1969).

A.T. Young, "Shadow Bands and the March Solar Eclipse—I," *Sky Telesc.* **39**, 176 (1970a).

A.T. Young, "Shadow Bands and the March Solar Eclipse—II," *Sky Telesc.* **40**, 242 (1970b).